Supporting information

Aptasensing of ractopamine in human plasma sample using gold electrode modified by poly (β-cyclodextrin) and dipenicillamine functionalized dendritic fibrous nanosilica (DFNS-DPA): An innovative sensitive quantification

Milad Baggal Bahyar, Nasrin Shadjou[*]

Department of Nanotechnology, Faculty of Science and Chemistry, Urmia University, Urmia, Iran.

Corresponding Author
E-mail address:
(*) n.shadjou@urmia.ac.ir
Tel: +98(44) 33363311

Synthesis of DFNS and its Functionalization by DPA

Preparation of KCC-1 and KCC-1-NH$_2$

KCC-1 was synthesized according to the methods which was reported by Bayal and coworkers [1]. Briefly, 1 g of CTAB was added to 10 mL distilled water and after addition of 0.6 g urea, the mixture was stirred for about 3 h at room temperature. Then, the mixture of 2 g TEOS, 30 mL cyclohexane and 1.5 mL hexanol was added to the flask and sonicated for 30 min. Afterwards, the mixture was heated at 80 ˚C for 4 h and subsequently refluxed at 80 ˚C for 24 h. Next, the mixture was cooled to the room temperature and centrifuged to collect the KCC-1 as white sediment. The collected KCC-1 was washed several times with water and ethanol and dried at 60 ˚C for 24 h. Finally, the as-synthesized KCC-1 was calcinated at 550 ˚C for 6 h to remove the CTAB as templating agent. As mechanism of the KCC-1 synthesis, urea was used to hydrolyze the TEOS to produce negatively charged $(SiO_4)^{-4}$ silicate. Using of CTAB induce the silicate molecules to form self-assembled linear structures where the CTAB help to the aggregating of the silicates [2, 3].

To functionalize the KCC-1 surface with NH$_2$ moieties, 0.02 g of KCC-1 was dispersed on 1.2 mL dried toluene and sonicated for 30 min. Then 50 μL 3-aminopropyltriethoxysilane (APTES) was added to the mixture and refluxed for 20 h at 80 ˚C. Then the mixture separated and washed with toluene several times and dried at 80 ˚C for at least 24 h. The surface morphology and porosity of the as-synthesized KCC-1 and KCC-1-NH$_2$ were approved by FE-SEM and BET.

Finally, dPA was conjugated to the dendritic fibers of KCC-1-NH$_2$ by EDC/NHS chemistry which provides the attaching of the dPA molecules at room temperature. Scheme S1 summurized all of the synthesized procedure.
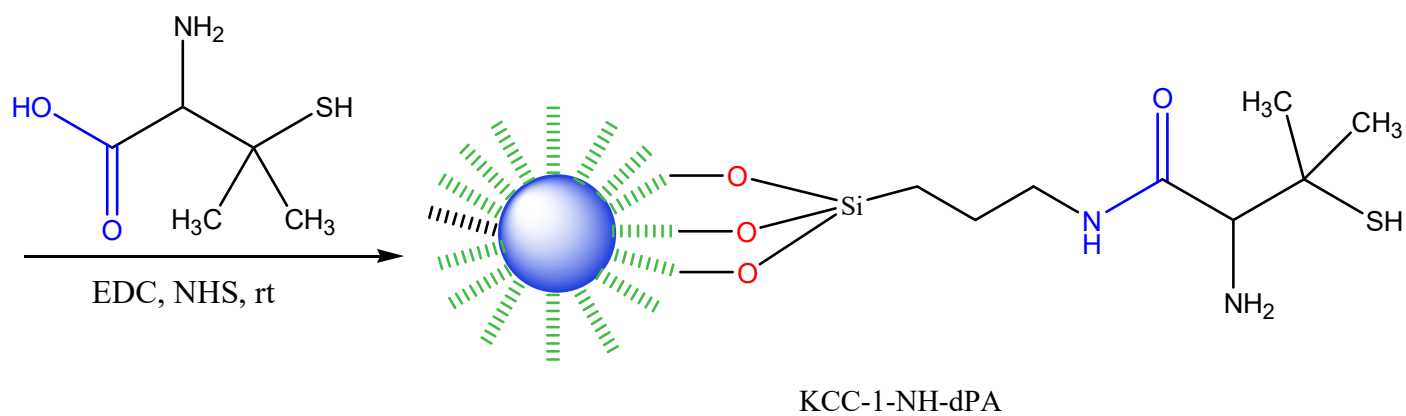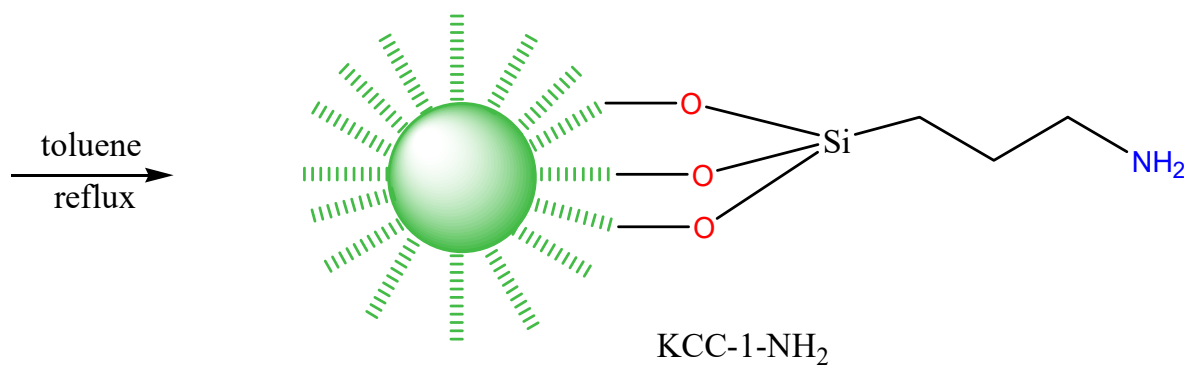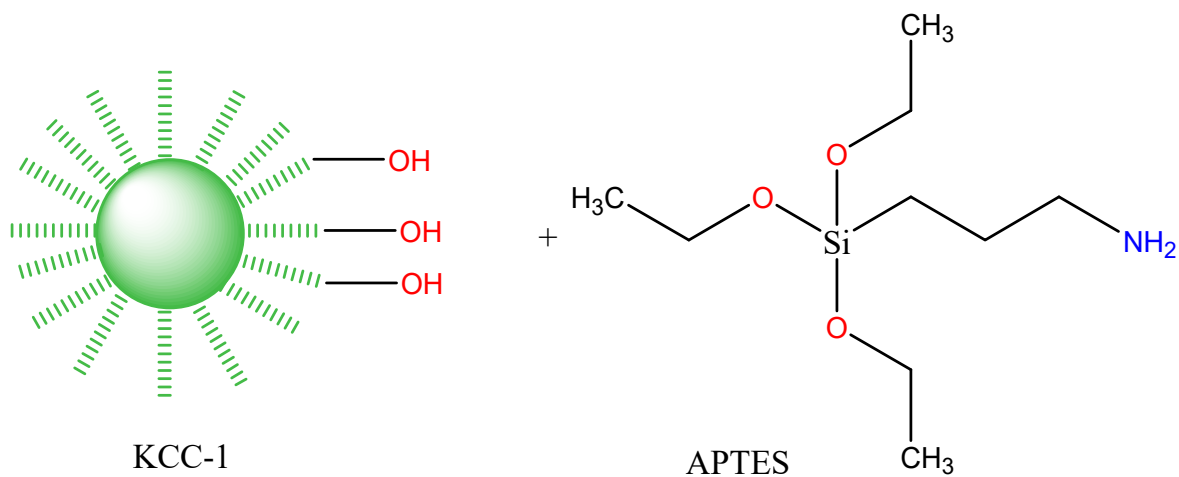
Scheme S1: Synthesized procedure of KCC-1-NH$_2$-dPA

Characterization of KCC-1, KCC-1-NH$_2$ and KCC-1-NH$_2$-dPA

TEM was used to further characterization of the KCC-1, KCC-1-NH$_2$ and KCC-1-NH$_2$-dPA (Fig. S1). The TEM images revealed the fibrous, porous and spiral shape of the nanomaterials which the fibrous form is as a result of using the CTAB for templating. Also, the particle sizes of KCC-1, KCC-1-NH$_2$ and KCC-1-NH$_2$-dPA are about 175, 190, and 200 nm, respectively.
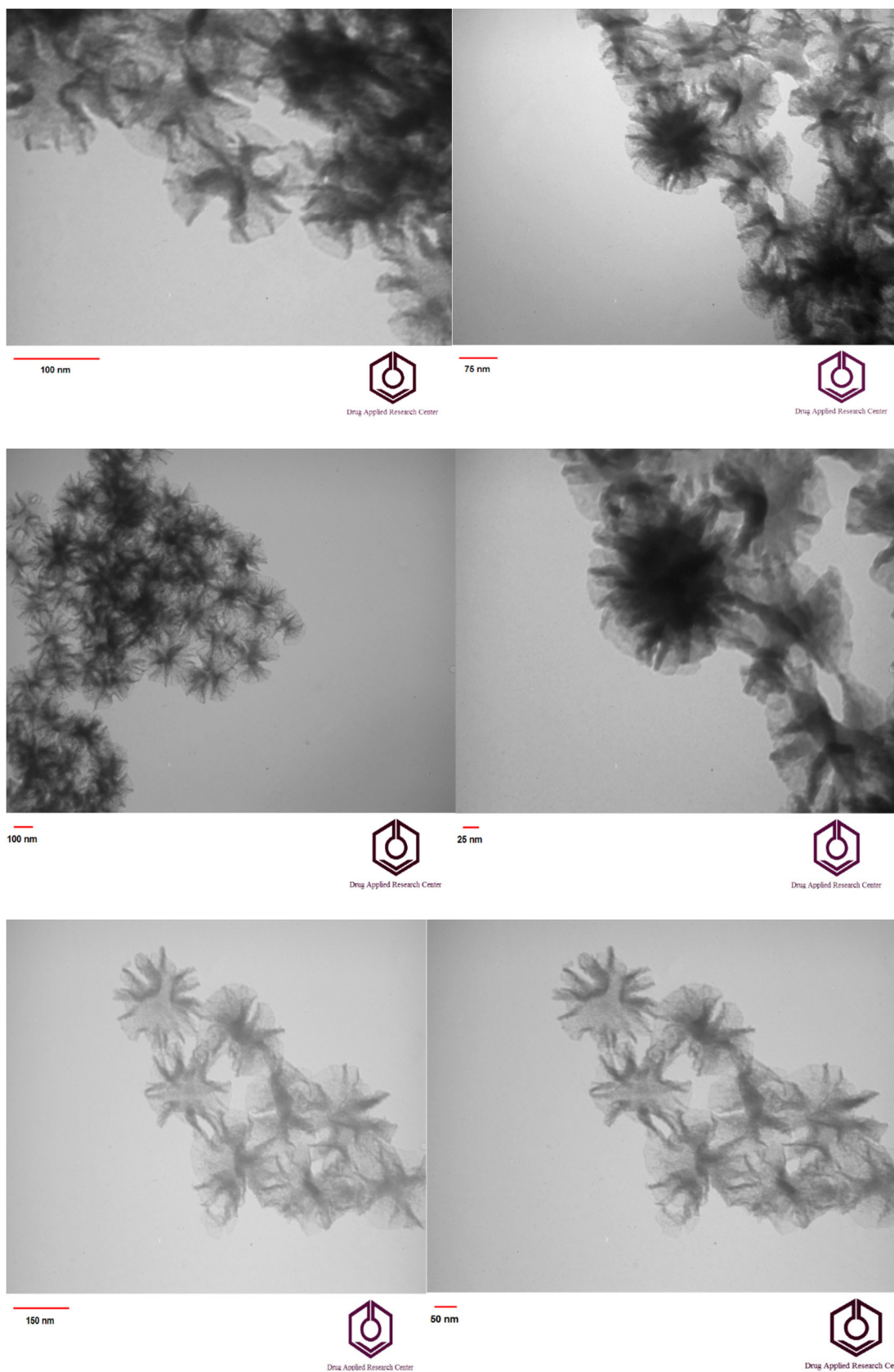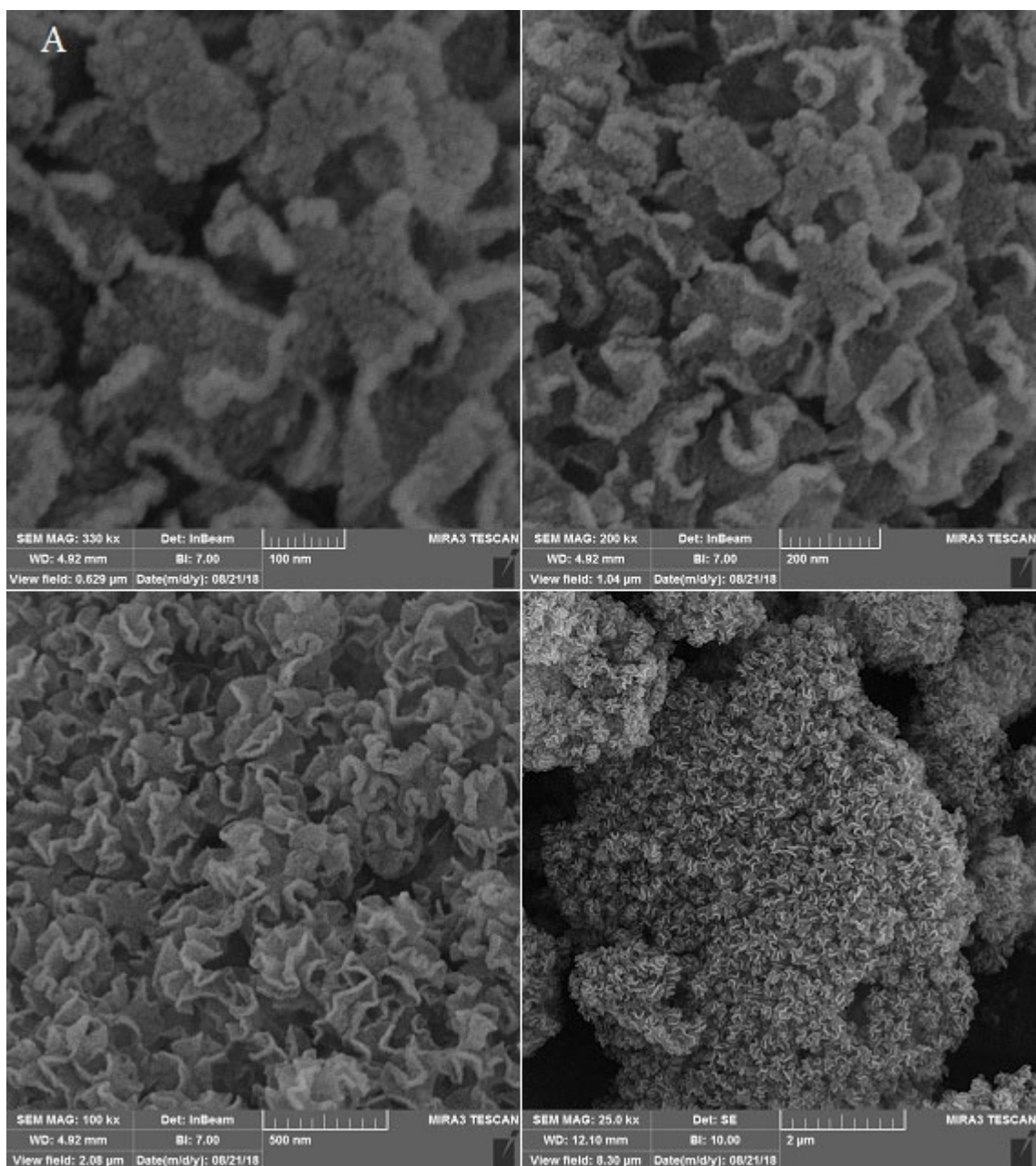
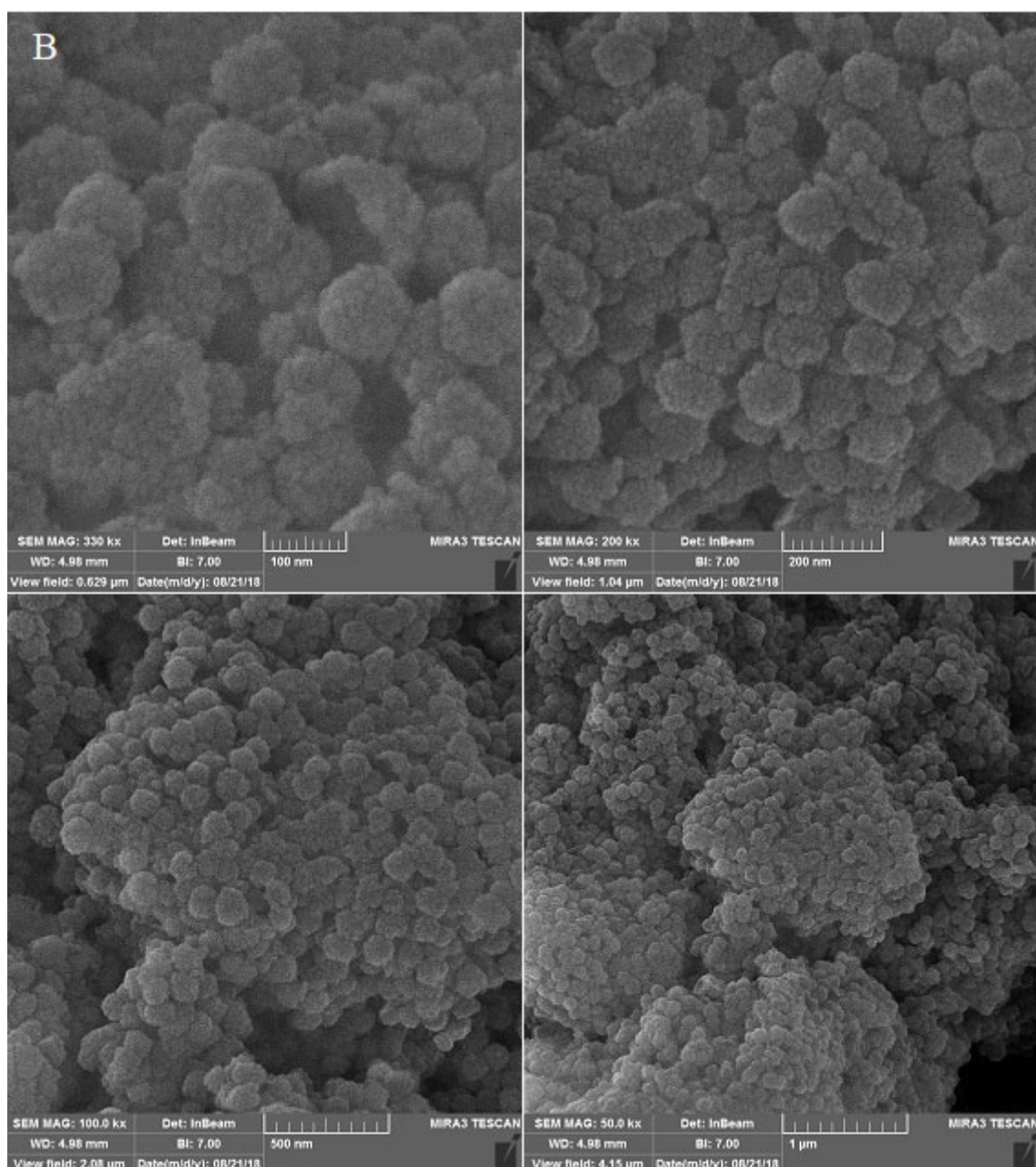**Fig. S1.** TEM images of KCC-1 (A), KCC-1-NH$_2$ (B) and KCC-1-NH$_2$-dPA (C).

Fig. S2, show the structural and morphological features of the KCC-1, KCC-1-NH_2 and KCC-1-NH_2-dPA using FE-SEM. The fibrous-sphere indicates the formation of KCC-1 based materials which the functionalization have no effect on the morphology of the KCC-1. EDX results reveal the atomic composition of the KCC-based materials where the KCC-1 is composed only with O and Si. However, the carbon is arising from the FE-SEM grid and the templating agent (Fig. S3). Upon functionalization with APTES, the weight percent of N, O and C are increased which imply the effective surface modification of KCC-1 with APTES.

FTIR was applied to approve the proper functionalization of the KCC-1 with –NH_2. As shown in Fig. S4, the characteristic peaks of the silica based materials could be observed in the range of 1020 to 1110 cm^{-1} representing the Si-O-Si asymmetric stretching and Si-OH peak is observed at 960 cm^{-1} which represents the stretching vibration and asymmetric bending.

The BET and BJH analyses of the KCC-1, KCC-1-NH_2 and KCC-1-NH_2-dPA were used to evaluate the porous nature of the nanoparticles. The specific surface area and porosity of the materials were determined using the adsorption isotherm and calculated by BET. BJH method was used to determine the pore volume of the KCC-1, KCC-1-NH_2 and KCC-1-NH_2-dPA. Table S1 lists the average pore size, surface area and pore volume of KCC-1, KCC-1-NH_2 and KCC-1-NH_2-dPA. The pore volumes were changed from 1.52 to 1.10 and 0.13 cm^3/g for KCC-1, KCC-1-NH_2 and KCC-1-NH_2-dPA, respectively. Also, surface area were obtained as 78.2, 367 and 617 m^2/g for KCC-1, KCC-1-NH_2, and KCC-1-NH_2-dPA, respectively. Mean pore diameter distribution of the materials were 9.87, 11.9 and 6.7 nm for KCC-1, KCC-1-NH_2 and KCC-1-NH_2-dPA, respectively (Fig. S5). The pore size, pore volumes and surface area of KCC-1, KCC-1-NH_2 and KCC-1-NH_2-dPA are obviously approved by the reported results [4,5].

Zeta potentials of KCC-1, KCC-1-NH$_2$ and KCC-1-NH$_2$-dPA were checked at pH 7.5 to determine the surface charge to conclude the possible surface modification. The KCC-1 bare fibrous nanomaterials display negative charge at pH 7.5 which could be resulted from Si-OH functional groups. However, the zeta potential of the KCC-1-NH$_2$ and KCC-1-NH$_2$-dPA show positive charges which confirms the anchoring amine and -SH groups on the surface of the fibrous materials, respectively. Also, DLS results of the KCC-1, KCC-1-NH$_2$ and KCC-1-NH$_2$-dPA show an increase on the hydrodynamic diameter of the nanomaterials from KCC-1 to KCC-1-NH$_2$-dPA which approve again the proper surface functionalization with NH$_2$ and FA groups. The XRD patterns of KCC-1, KCC-1-NH$_2$ and KCC-1-NH$_2$-dPA were performed from 3.0° (2θ) to 70.0° (2θ) (Fig. S6) to test the crystallinity of the produced KCC-1 based nanomaterials where two major peak could be observed which the crystallinity increased from KCC-1 to KCC-1-NH$_2$-dPA. The broad peak from 20° and 30° is assigned to the amorphous silica [6]. Also, compared to the KCC-1, the KCC-1-NH$_2$ and KCC-1-NH$_2$-dPA patterns were shifted to the higher 2θ values which is a reason for the surface functionalization of KCC-1.
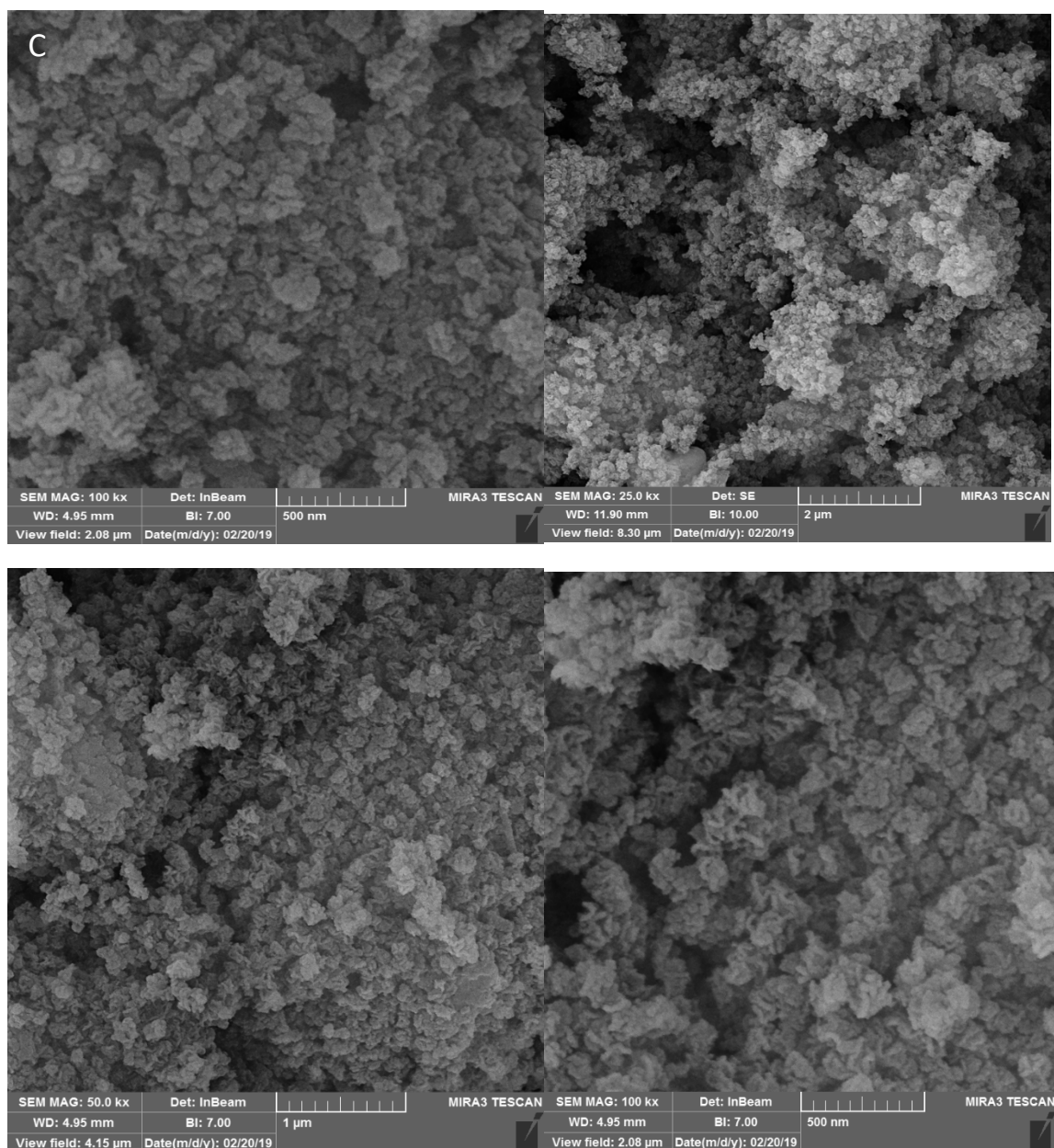
A

SEM MAG: 330 kx | Det: InBeam | | | | | | | | | | | | | MIRA3 TESCAN
WD: 4.92 mm | BI: 7.00 | 100 nm
View field: 0.629 μm | Date(m/d/y): 08/21/18

SEM MAG: 200 kx | Det: InBeam | | | | | | | | | | | | MIRA3 TESCAN
WD: 4.92 mm | BI: 7.00 | 200 nm
View field: 1.04 μm | Date(m/d/y): 08/21/18

SEM MAG: 100 kx | Det: InBeam | | | | | | | | | | | | MIRA3 TESCAN
WD: 4.92 mm | BI: 7.00 | 500 nm
View field: 2.08 μm | Date(m/d/y): 08/21/18

SEM MAG: 25.0 kx | Det: SE | | | | | | | | | | | | MIRA3 TESCAN
WD: 12.10 mm | BI: 10.00 | 2 μm
View field: 8.30 μm | Date(m/d/y): 08/21/18

B

SEM MAG: 330 kx	Det: InBeam	100 nm	MIRA3 TESCAN
WD: 4.98 mm	BI: 7.00		
View field: 0.629 µm	Date(m/d/y): 08/21/18		

SEM MAG: 200 kx	Det: InBeam	200 nm	MIRA3 TESCAN
WD: 4.98 mm	BI: 7.00		
View field: 1.04 µm	Date(m/d/y): 08/21/18		

SEM MAG: 100.0 kx	Det: InBeam	500 nm	MIRA3 TESCAN
WD: 4.98 mm	BI: 7.00		
View field: 2.08 µm	Date(m/d/y): 08/21/18		

SEM MAG: 50.0 kx	Det: InBeam	1 µm	MIRA3 TESCAN
WD: 4.98 mm	BI: 7.00		
View field: 4.15 µm	Date(m/d/y): 08/21/18		

Fig. S2. FE-SEM images of KCC-1 (A), KCC-1-NH$_2$ (B) and KCC-1-NH$_2$-dPA (C).
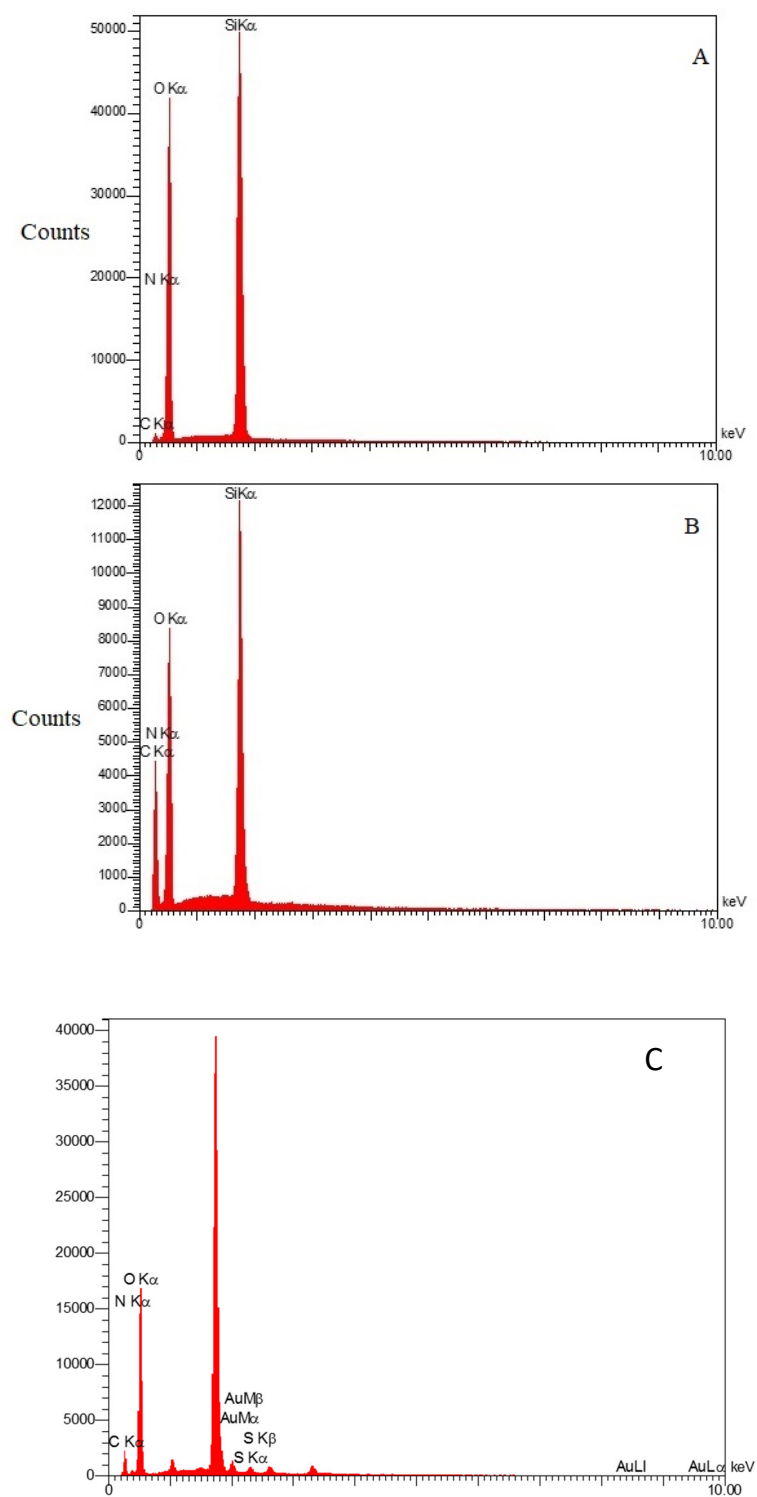
Fig. S3. EDX analysis of KCC-1 (A), KCC-1-NH$_2$ (B) and KCC-1-NH$_2$-dPA (C).
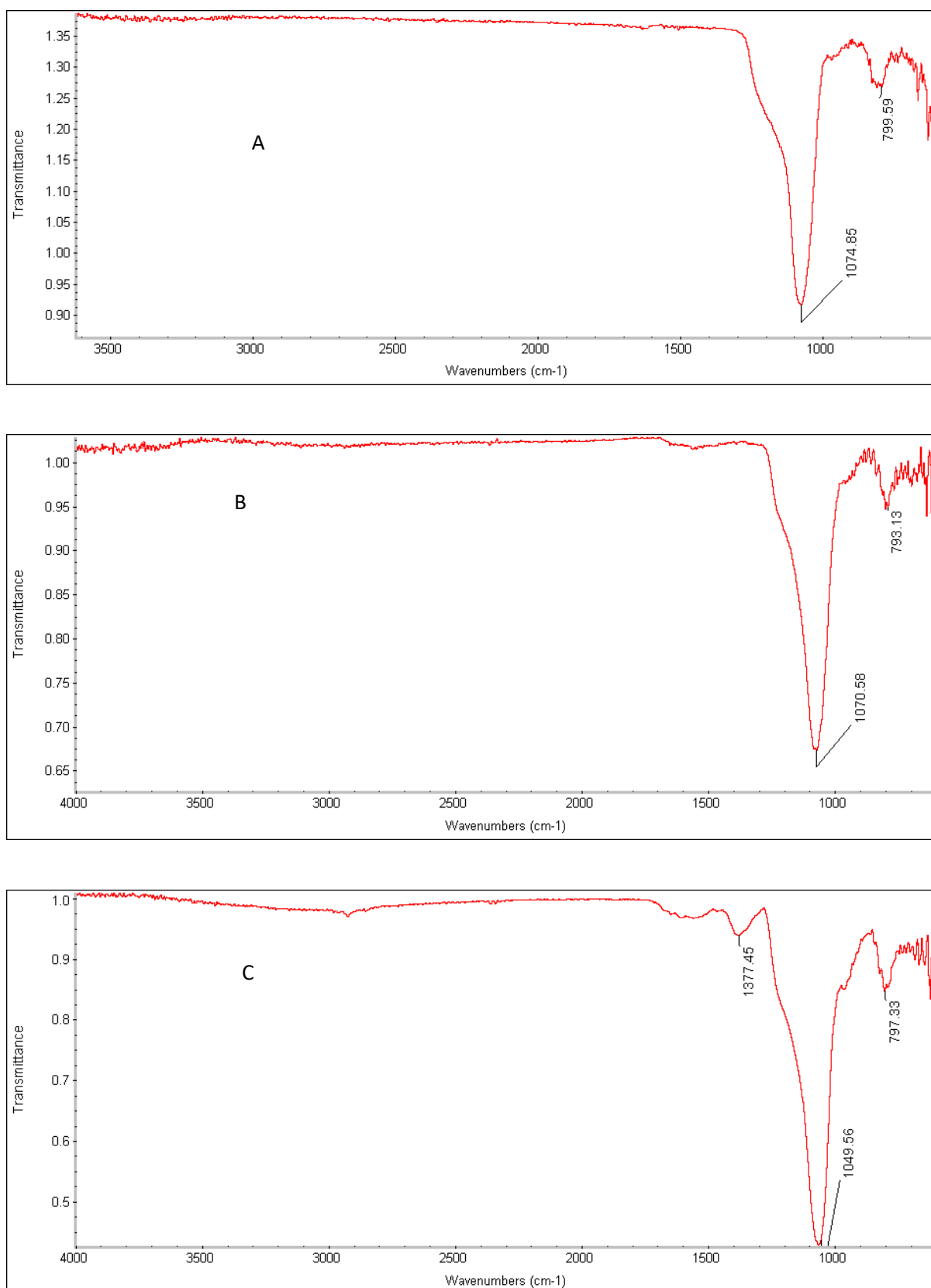
Fig. S4. FT-IR Spectra of KCC-1 (A), KCC-1-NH_2 (B) and KCC-1-NH_2-dPA (C).
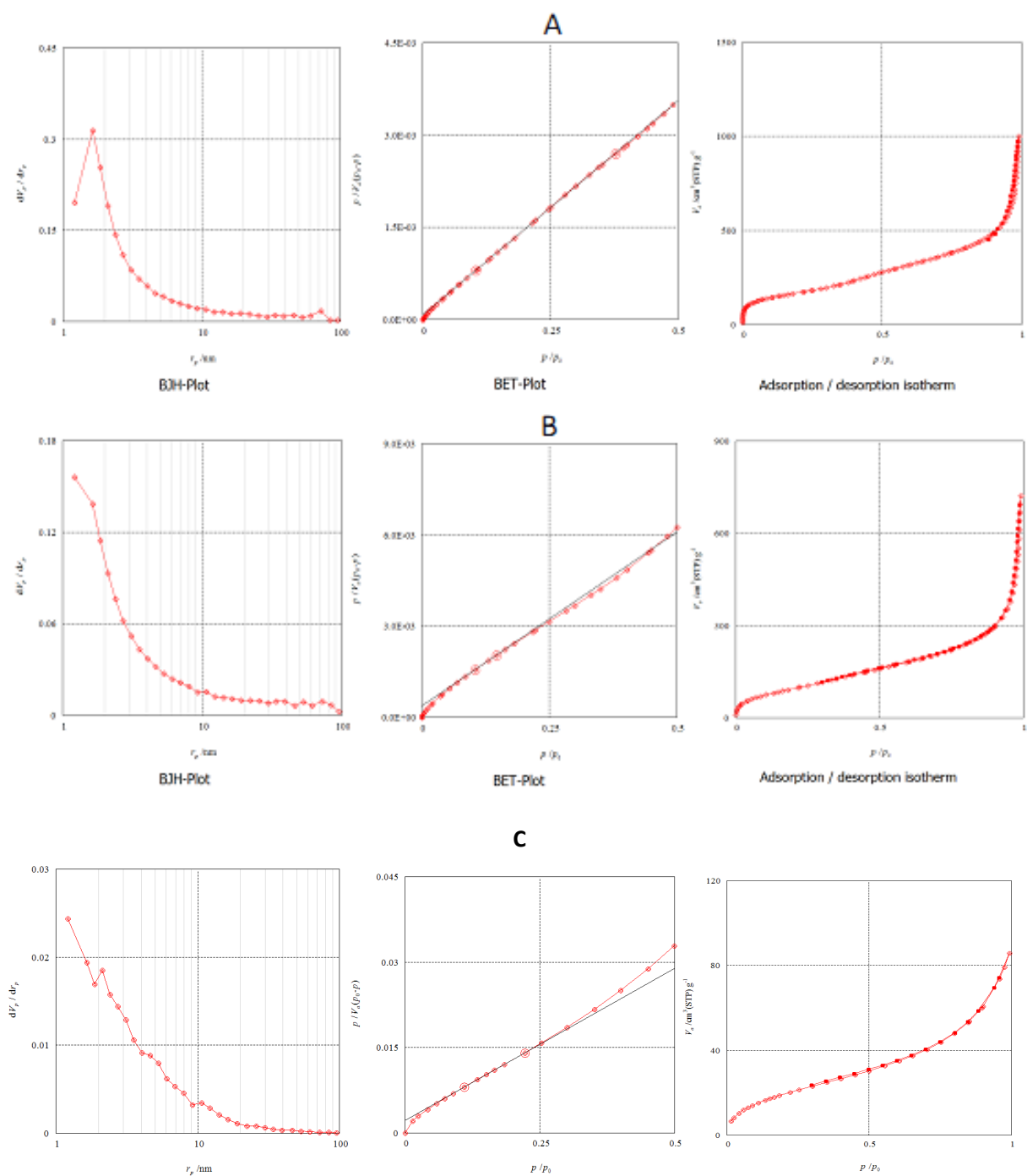
Fig. S5. BJH, BET and nitrogen adsorption/desorption isotherm of KCC-1 (A), KCC-1-NH$_2$ (B) and KCC-1-NH$_2$-dPA (C). (P/P^0 = relative pressure (surface pressure/preliminary pressure)).

Table. S1. Surface area, average pore size, and pore volume of KCC-1, KCC-1-NH$_2$ and KCC-1-NH$_2$-dPA.

Material type	Pore size (nm)[a]	Pore volume (cm^3 g^{-1})[b]	Surface Area (m^2 g^{-1})
KCC-1	9.87	1.52	617
KCC-1-NH$_2$	11.99	1.10	367
KCC-1-NH$_2$-dPA	6.7	0.13	78.2

a Pore size was calculated by BET. b Pore volume determined by BJH.
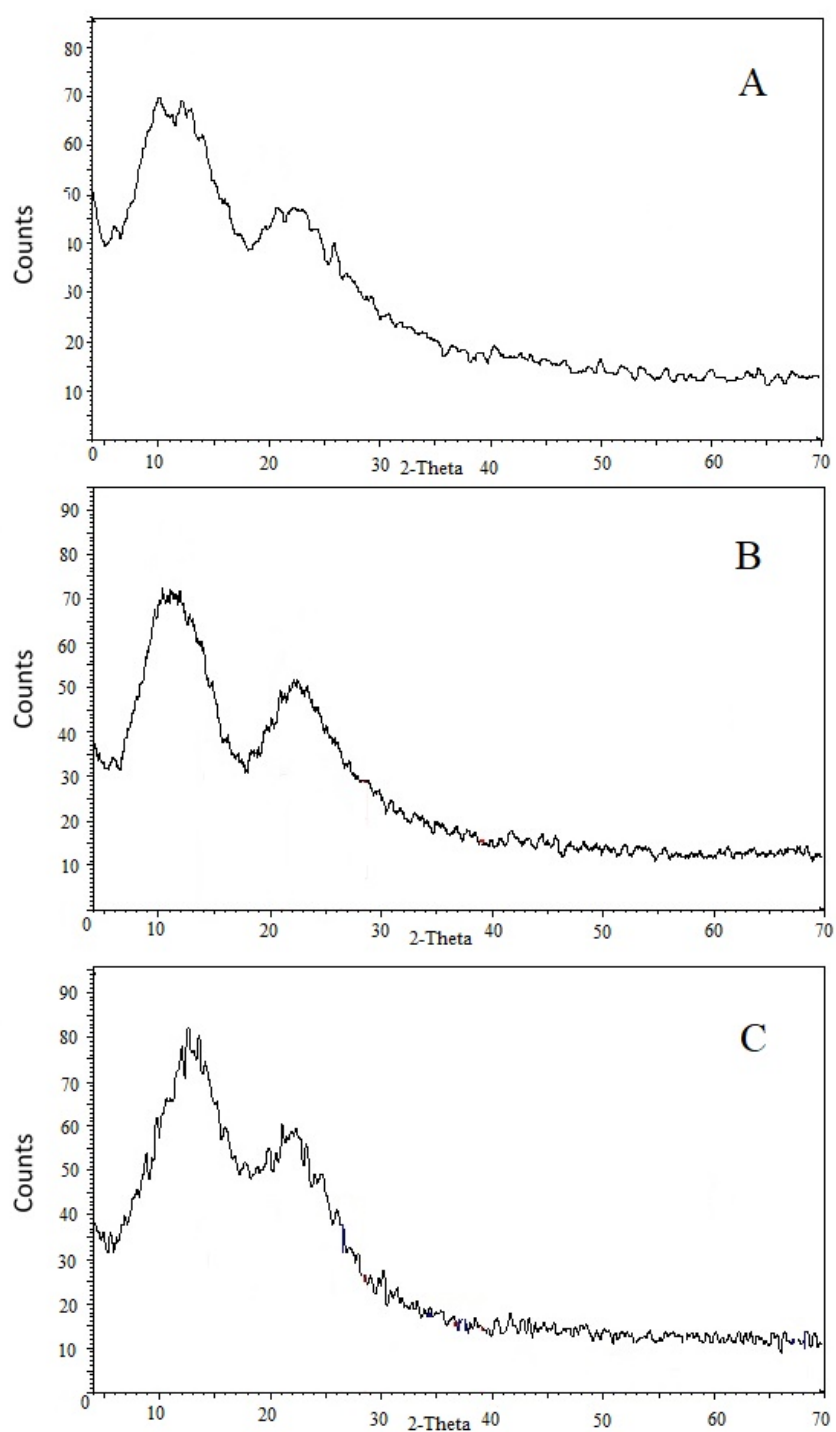
Fig. S6. XRD analysis of KCC-1 (A), KCC-1-NH$_2$ (B) and KCC-1-NH$_2$-dPA (C).
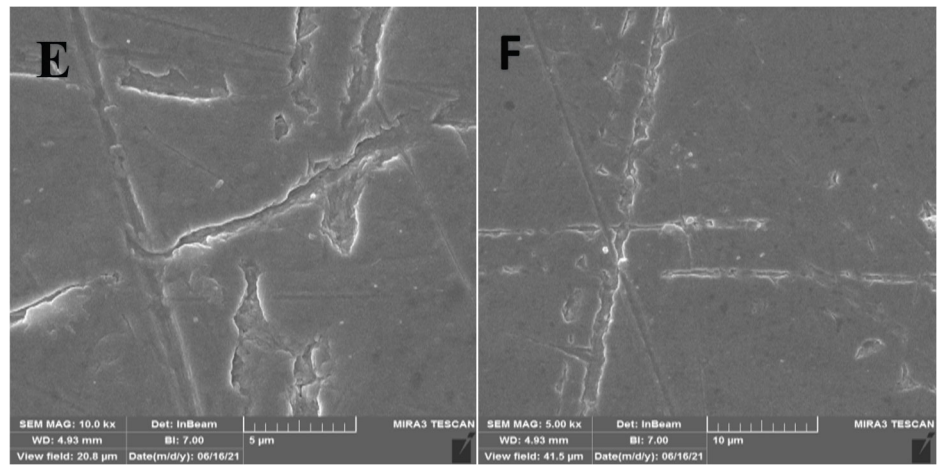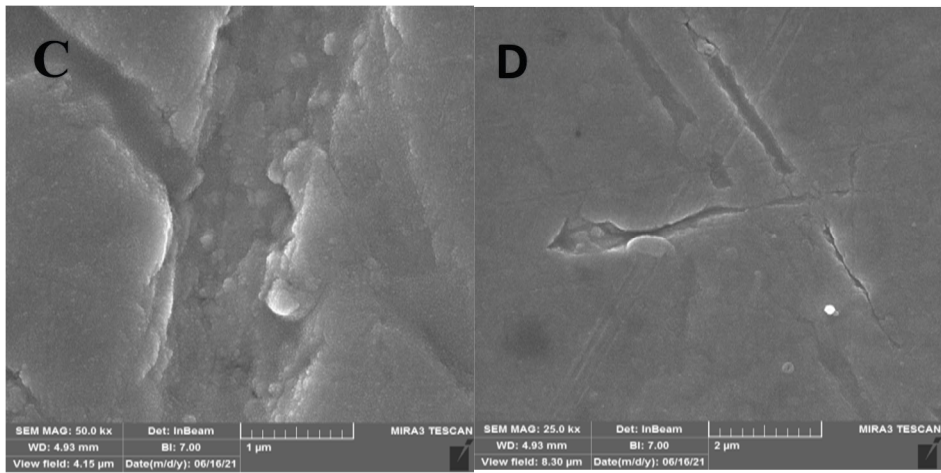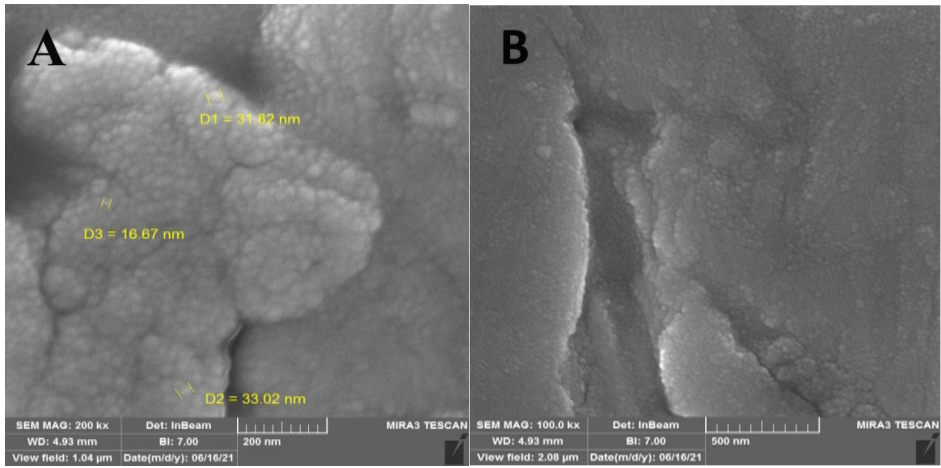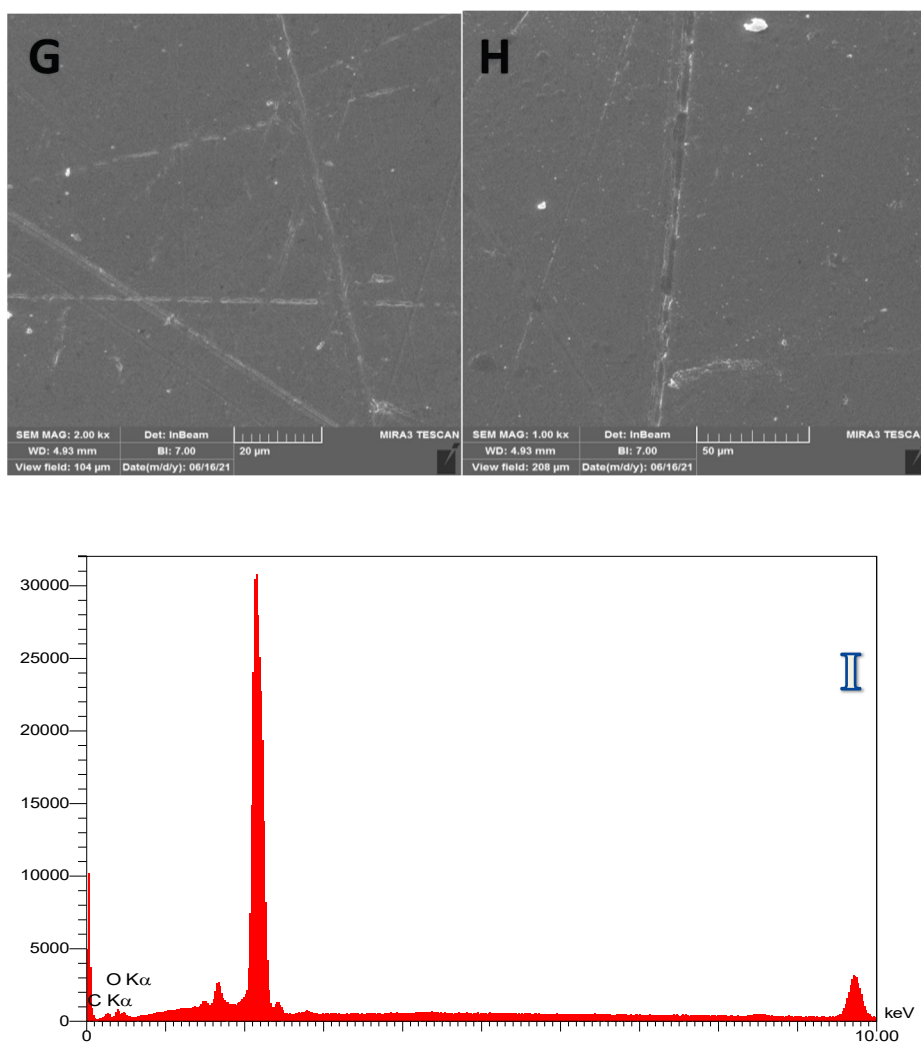
Figure S7. A-H) FE-SEM of P (β-CD)/Au electrode in different magnifications and **I)** EDS of P (β-CD)/Au electrode.
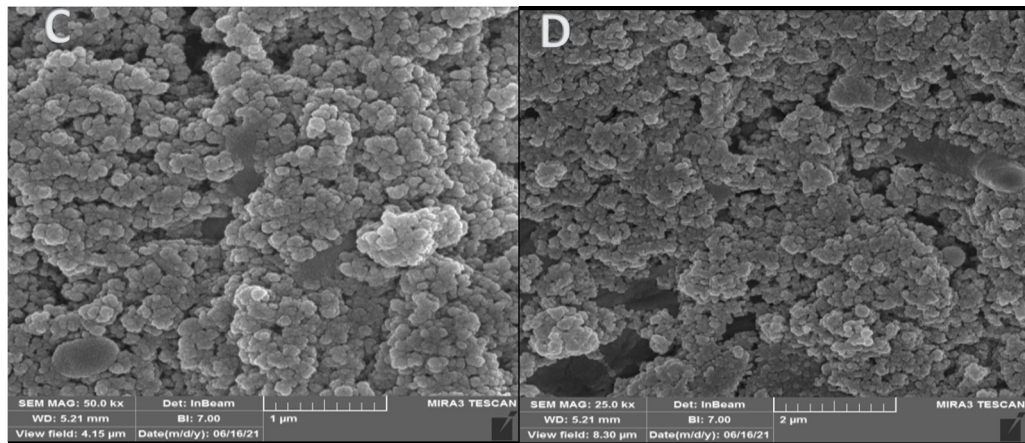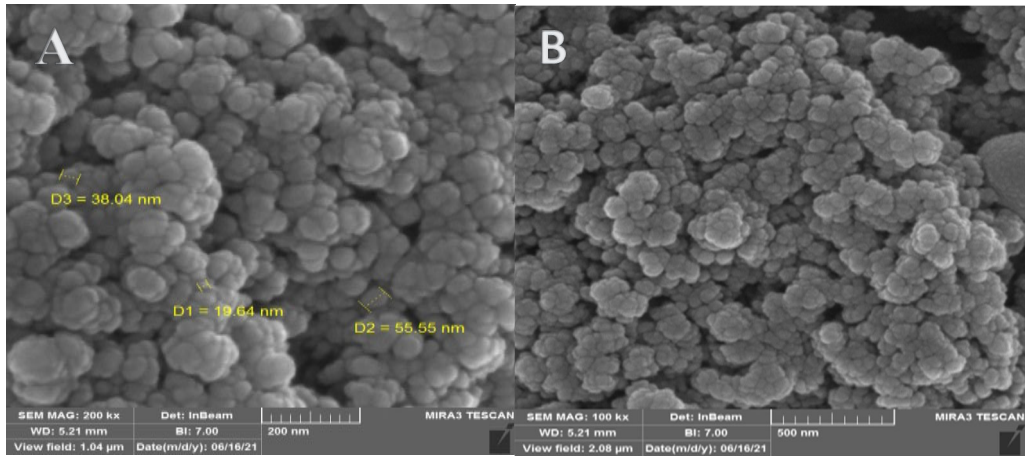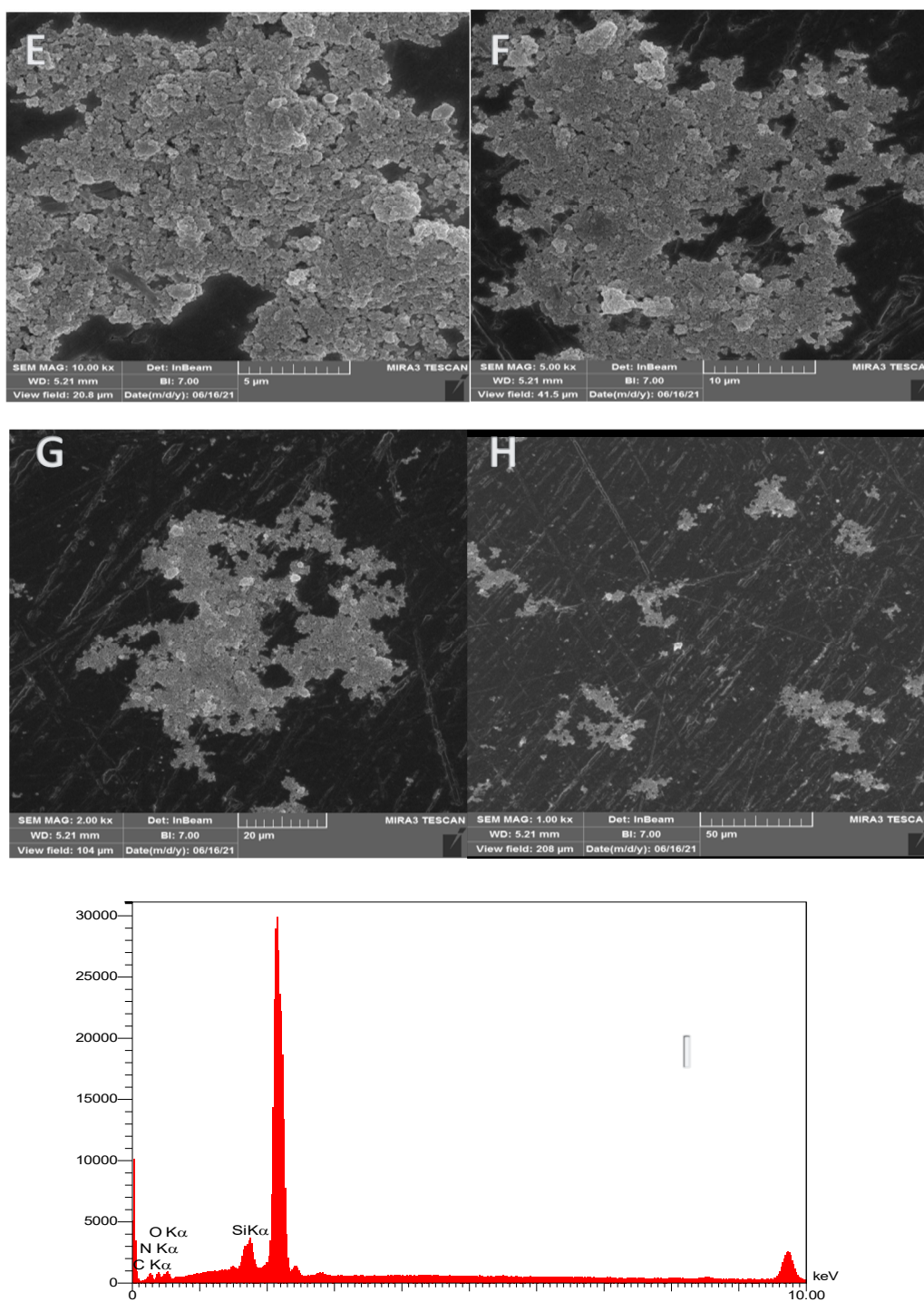
Figure S8. A-H) FE-SEM image of KCC-1-NH$_2$-DPA/P (β-CD)/Au electrode in different magnifications and **I)** EDS for of KCC-1-NH$_2$-DPA/P (β-CD)/Au electrode.
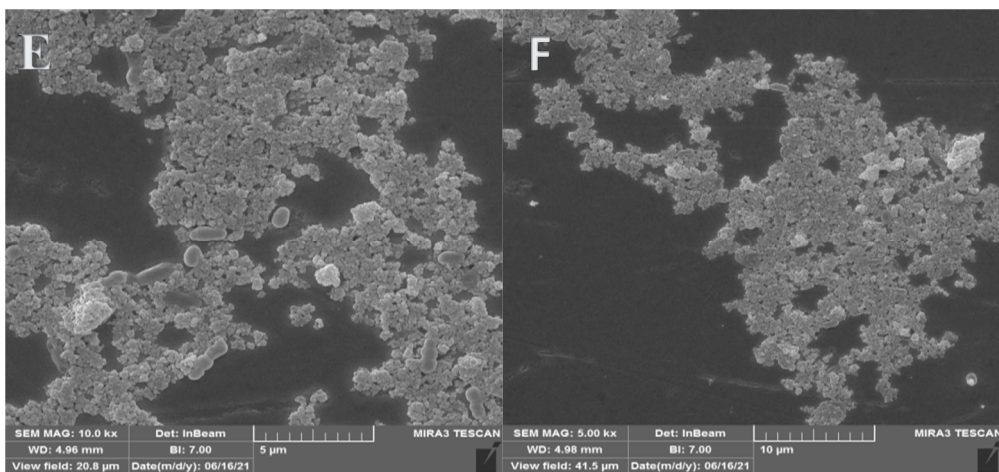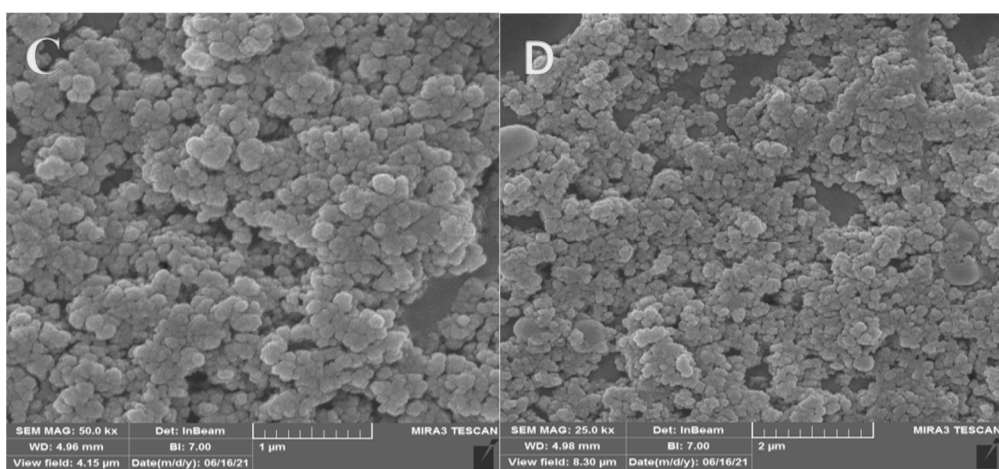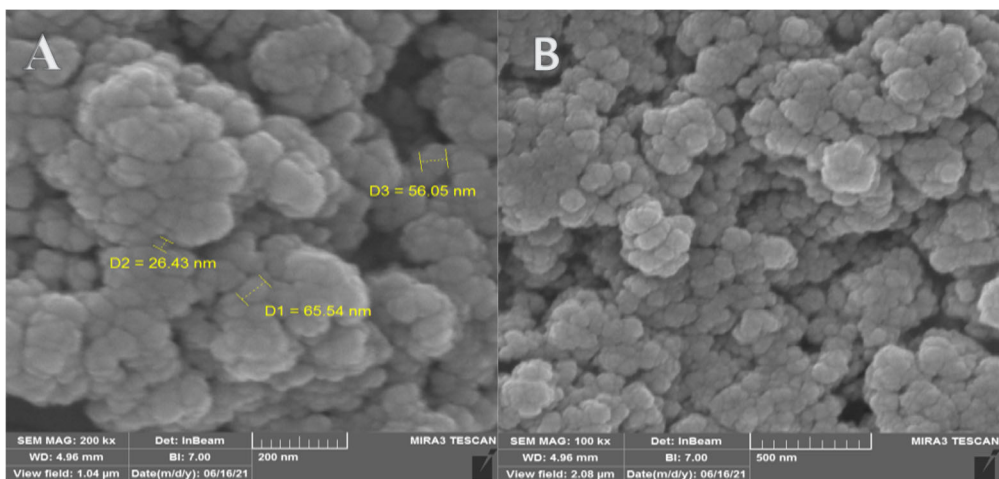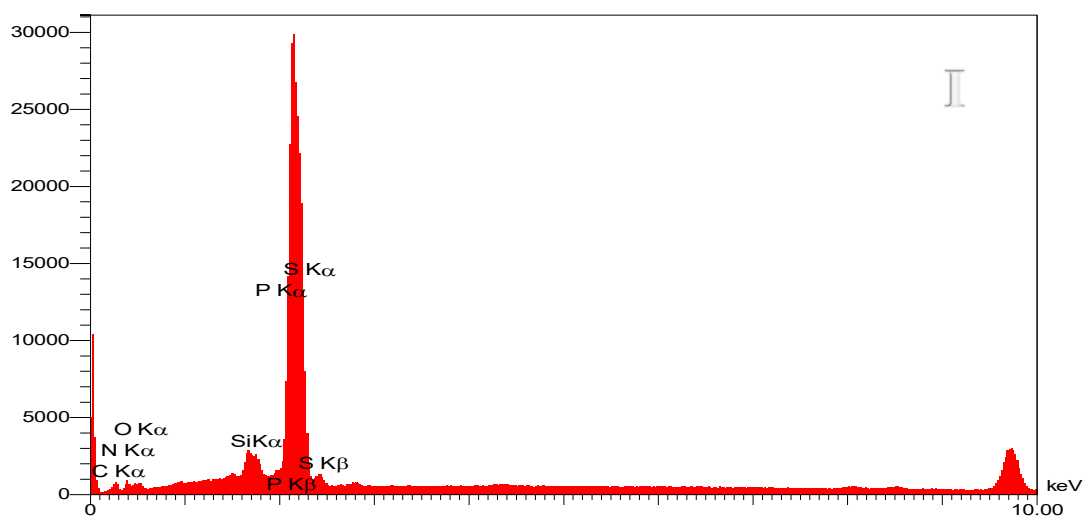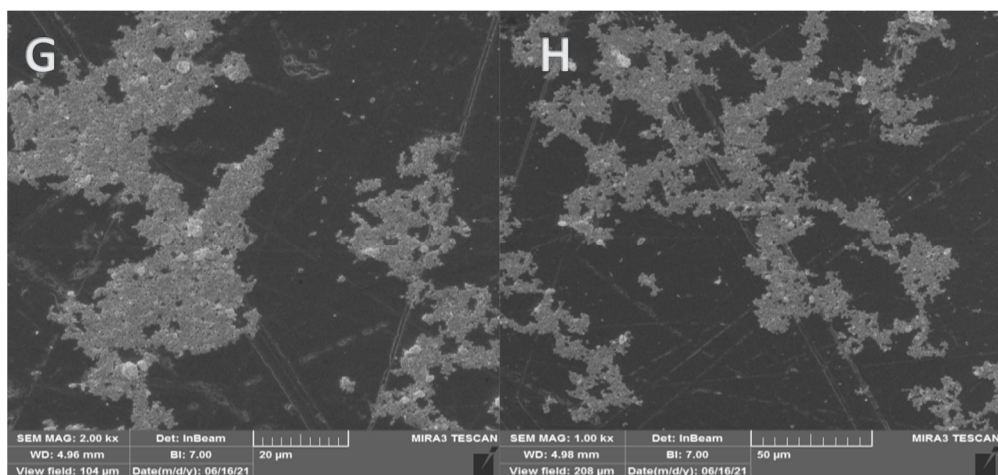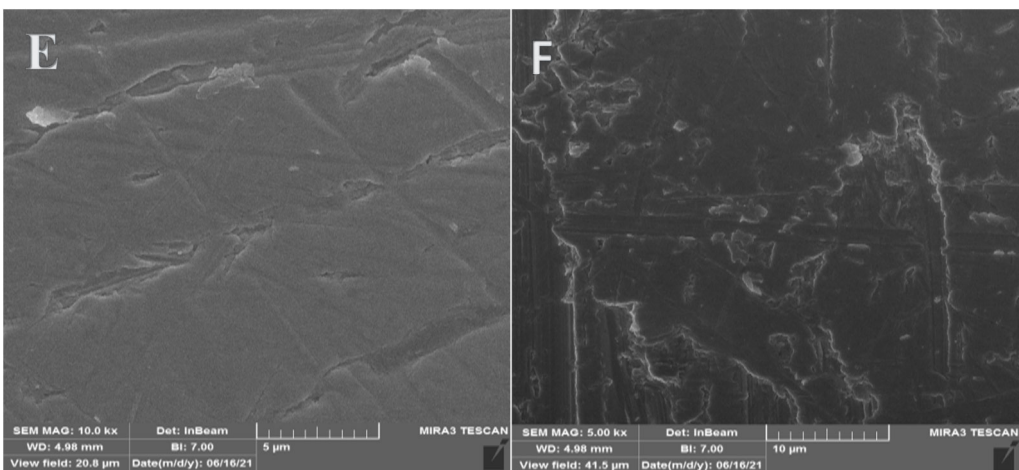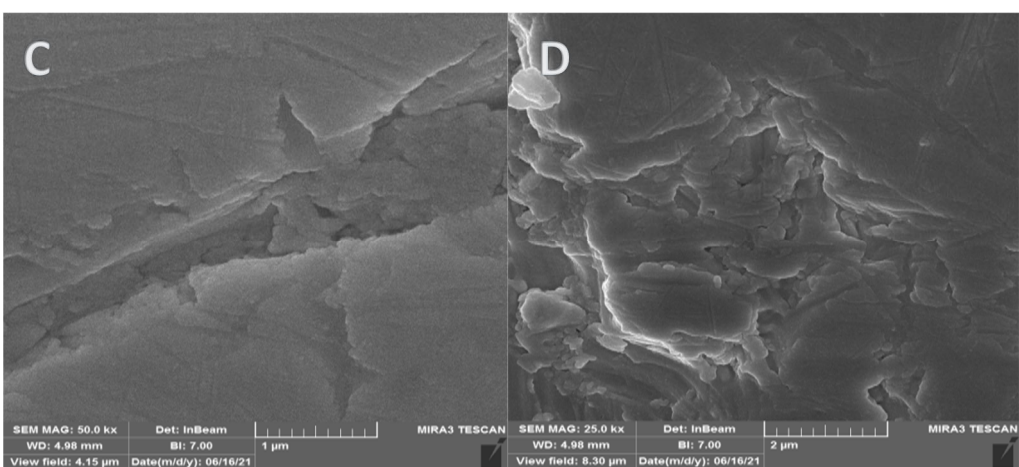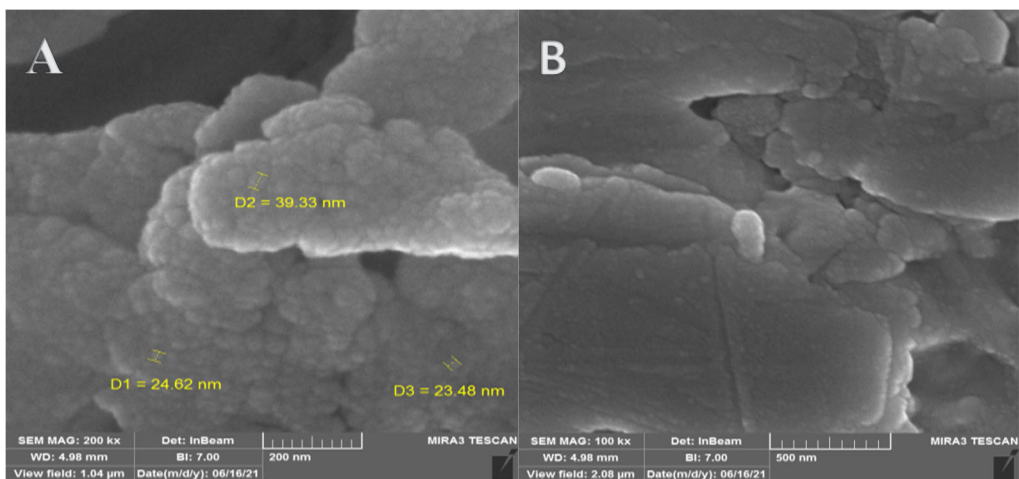
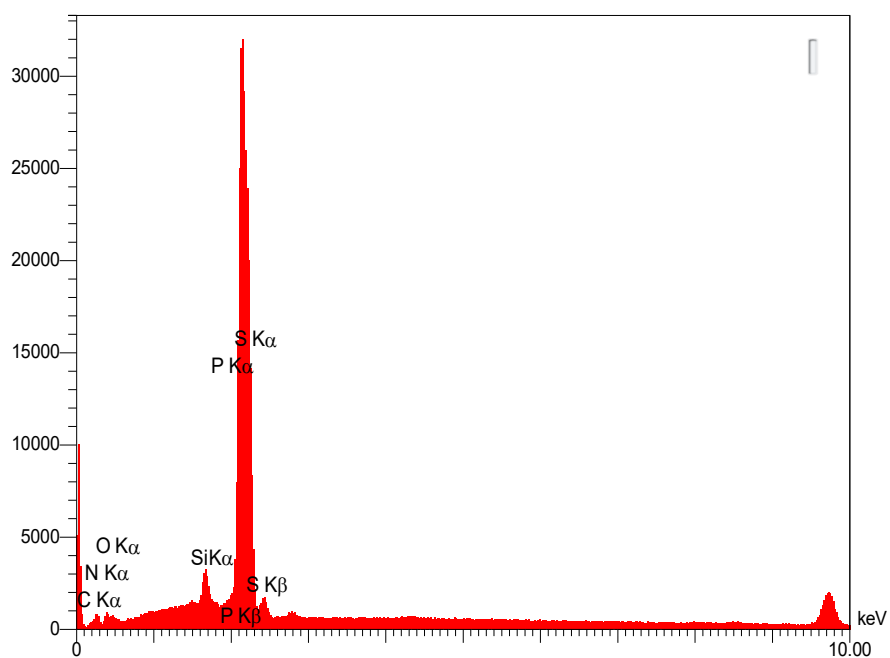**Figure S9. A-H)** FE-SEM image of aptamer/KCC-1-NH$_2$-DPA/P (β-CD)/Au electrode in different magnifications and **I)** EDS for of aptamer/KCC-1-NH$_2$-DPA/P (β-CD)/Au electrode.

Figure S10. A-F) FE-SEM image of RAC/aptamer/KCC-1-NH$_2$-DPA/P (β-CD)/Au electrode in different magnifications and **G)** EDS for of RAC/aptamer/KCC-1-NH$_2$-DPA/P (β-CD)/Au electrode.
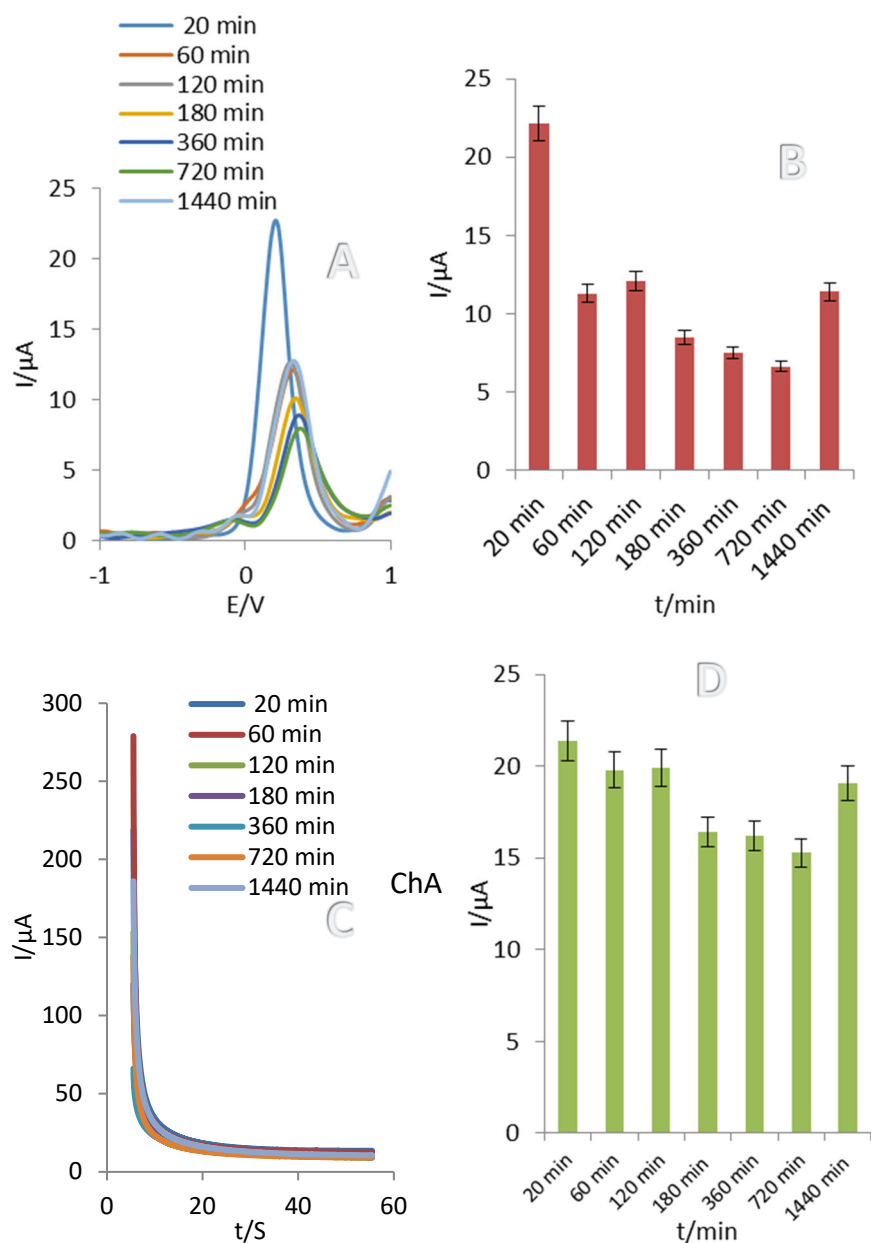
Figure S11. A-B) DPVs of aptamer/KCC-1-NH$_2$-DPA/P (β-CD)/Au electrode in different incubation time of aptamer (20, 60, 120, 180, 360 and 720 min) at a potential range of -1 to +1 V in 0.01M [Fe(CN)$_6$]$^{3-/4-}$/KCl solution as electrochemical probe and histogram of peak current *versus* time (n=3, SD=1.29). **C-D)** ChAs of aptamer incubation time on the KCC-1-NH$_2$-DPA/P (β-CD)/Au electrode with calibration curves at the potential of 0.5V during 50 seconds (n=3, SD=2.04).
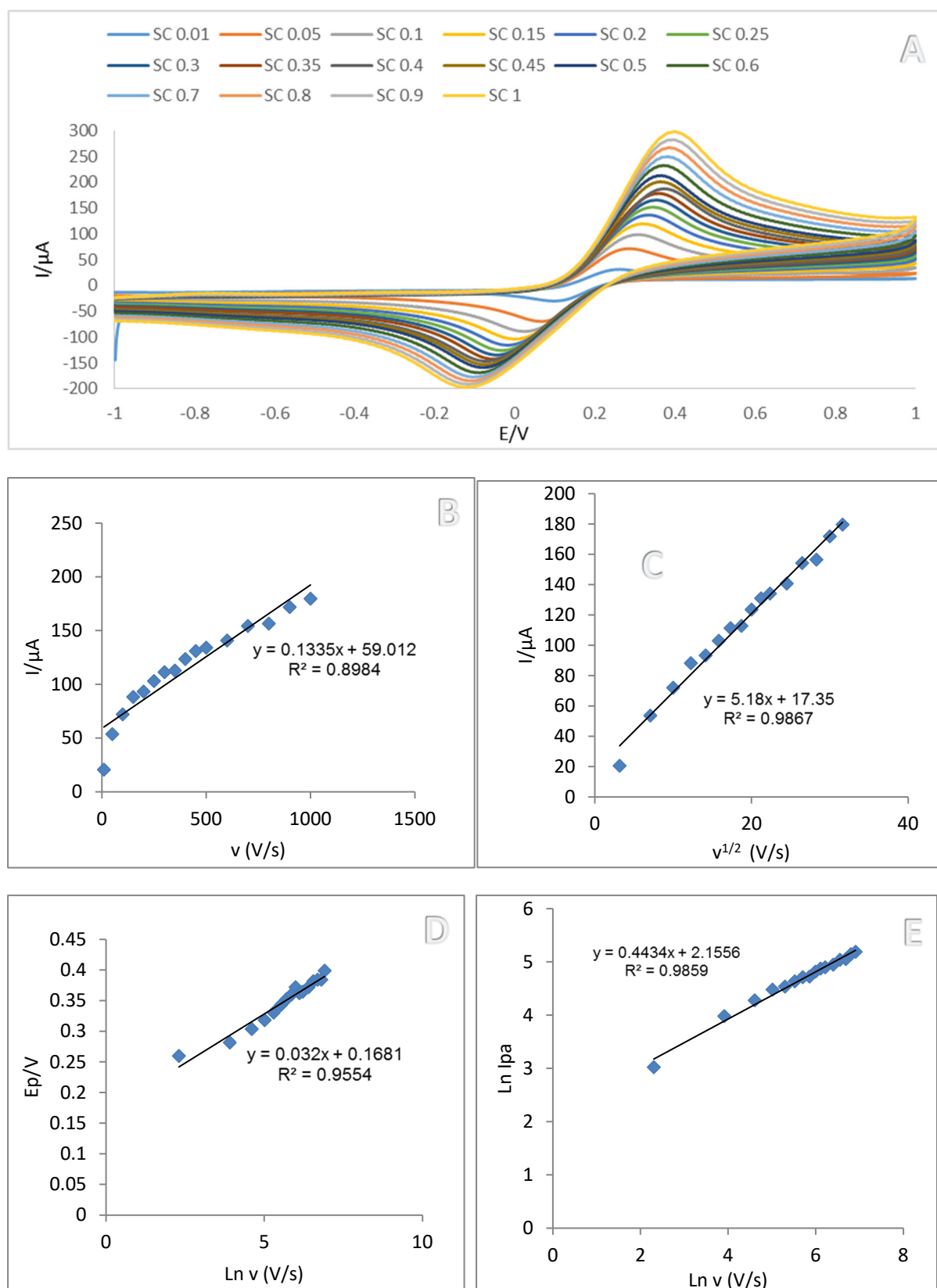
Figure S12. A) CVs of KCC-1-NH₂-DPA/P (β-CD)/Au electrode at the potential range -1 to

+1 V with different scan rate (10, 50, 100, 150, 200, 250,300, 350, 400, 450, 500, 600, 700,

800, 900 and 1000 mV / s) in 0.01 M $[Fe(CN)_6]^{3-/4-}$/KCl solution as electrolyte support. **B)** Variations of oxidation peak currents versus different sweep rate. **C)** Variations of oxidation peak currents versus square root of different sweep rate. **D)** Variation of oxidation peak potential versus Neperian logarithm of sweep rate. **E)** Calibration curve of oxidation peak's current versus sweep rate in terms of Neperian logarithm.
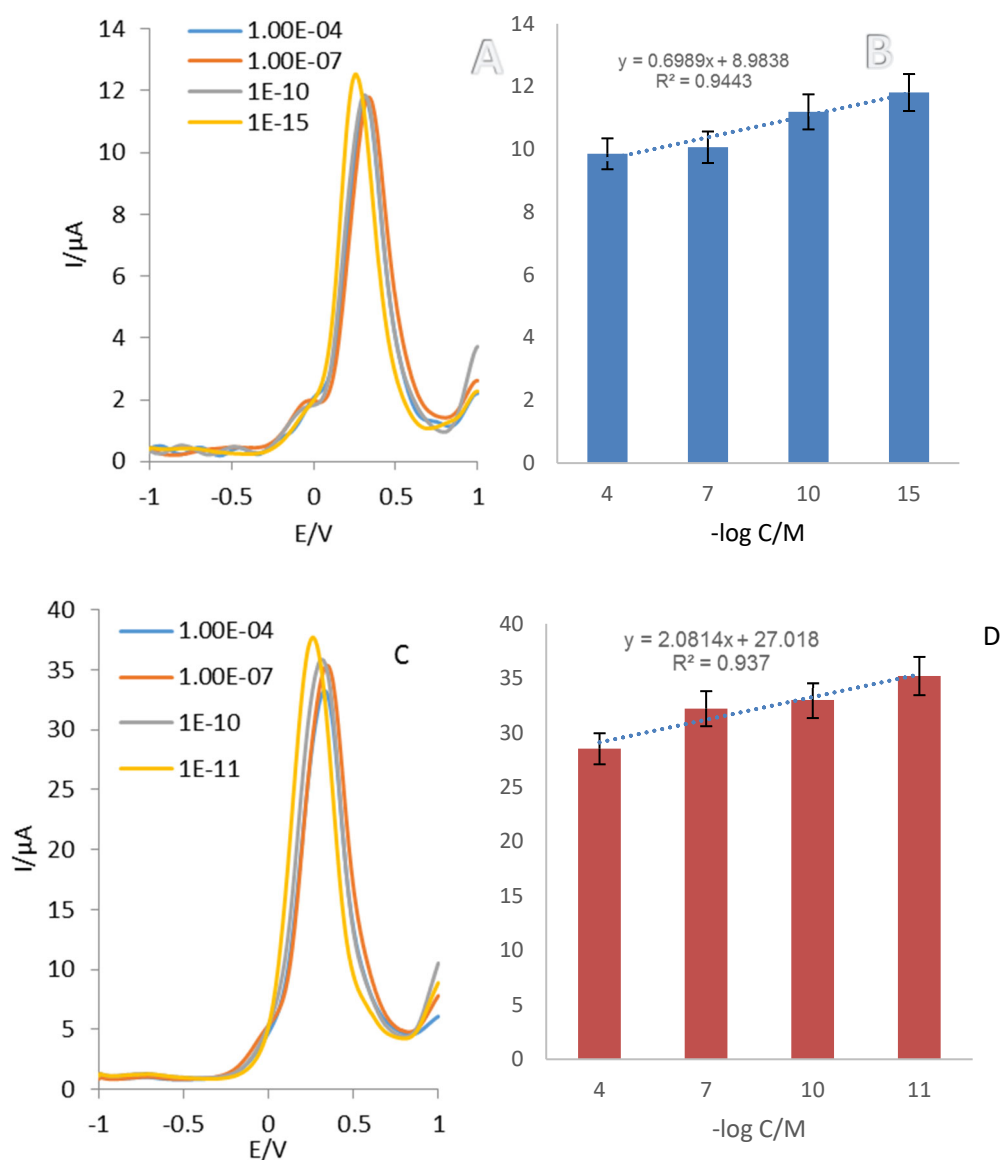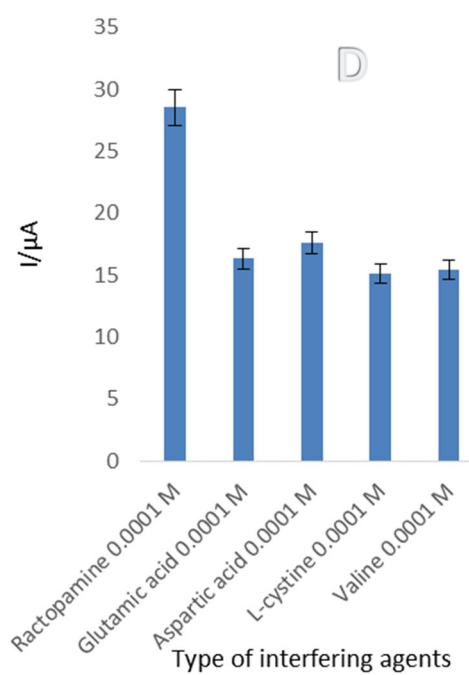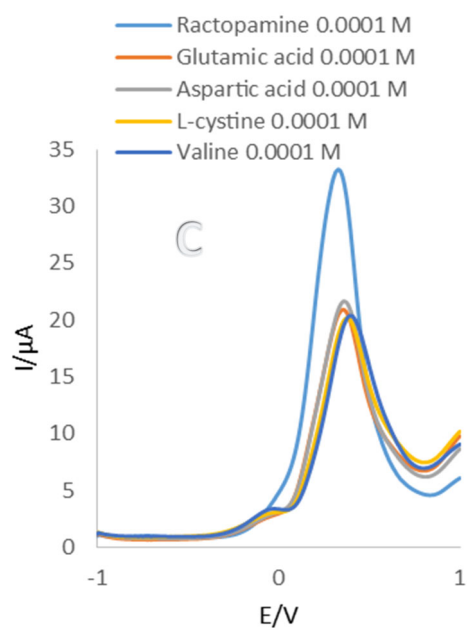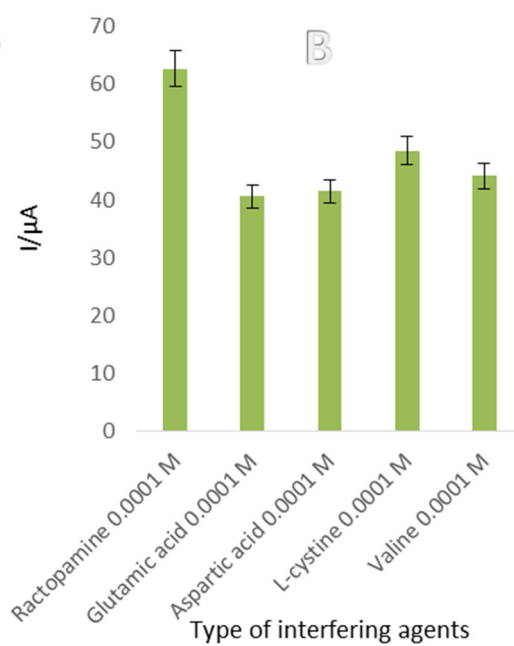
Figure S13. A) DPVs and **C)** SWVs of developed aptasensor on the present of different concentrations (1×10^{-4} , 1×10^{-5} , 1×10^{-6} , 1×10^{-7} , 1×10^{-8} , 1×10^{-9} , 1×10^{-10} M, 1×10^{-11} , 1×10^{-12} , 1×10^{-13} , 1×10^{-14} , 1×10^{-15} and 1×10^{-16} M) of RAC in the presence of 0.01 M $[Fe(CN)_6]^{3-/4-}$ /KCl 0.01 M as a support electrolyte. **B and D)** Calibration curves obtained by DPVs and SWVs techniques, respectively. (n=3, SD=2.26).
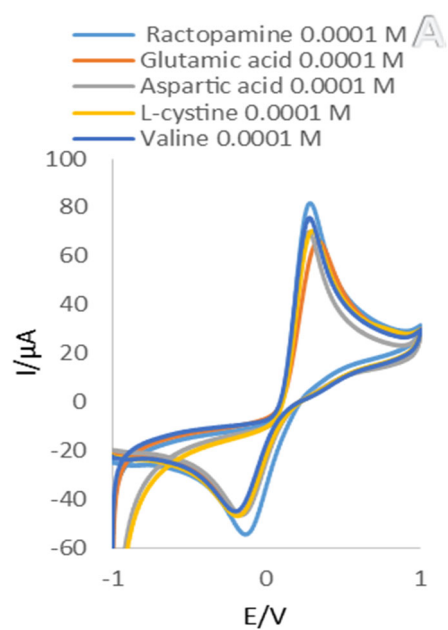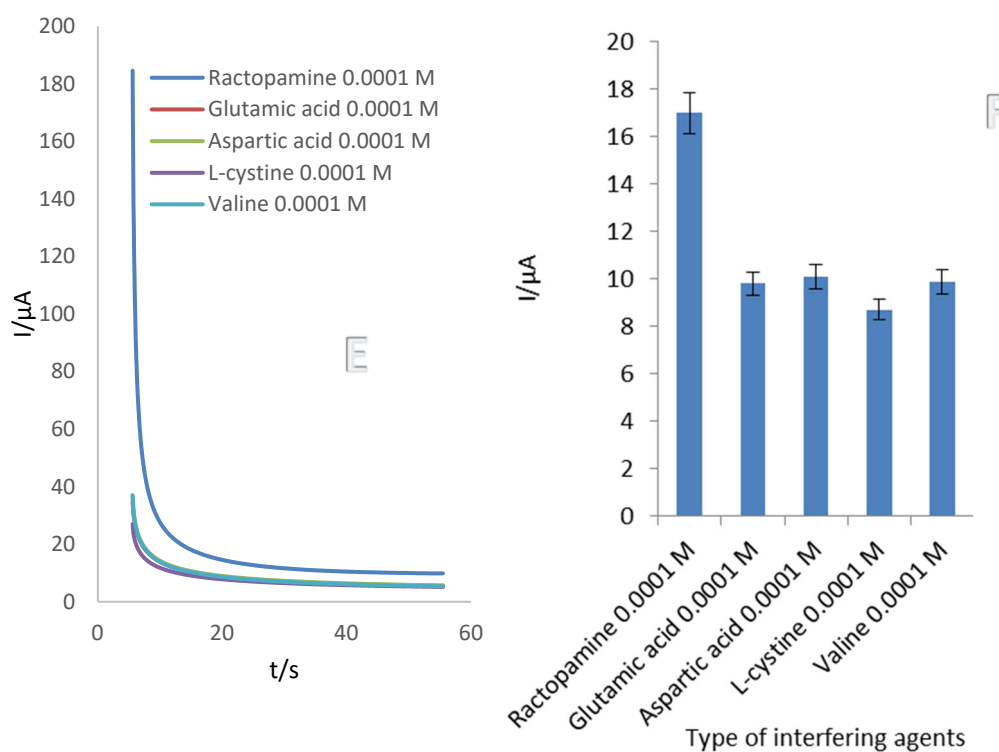
Figure S14. A-F) CVs, SWVs and ChAs of apta-platform in the presence of RAC (0.0001 M), glutamic acid (0.0001 M), aspartic acid (0.0001 M), L-cysteine (0.0001 M) and valine (0.0001 M) 0.01 M $[Fe(CN)_6]^{3-/4-}$/KCl 0.01 M solution is support electrolyte with histogram of peak current *versus* type of interfering species. (n=3, SD=1.29 for CV), (n=3, SD=1.06 for DPV), and (n=3, SD=1.12 for ChA).

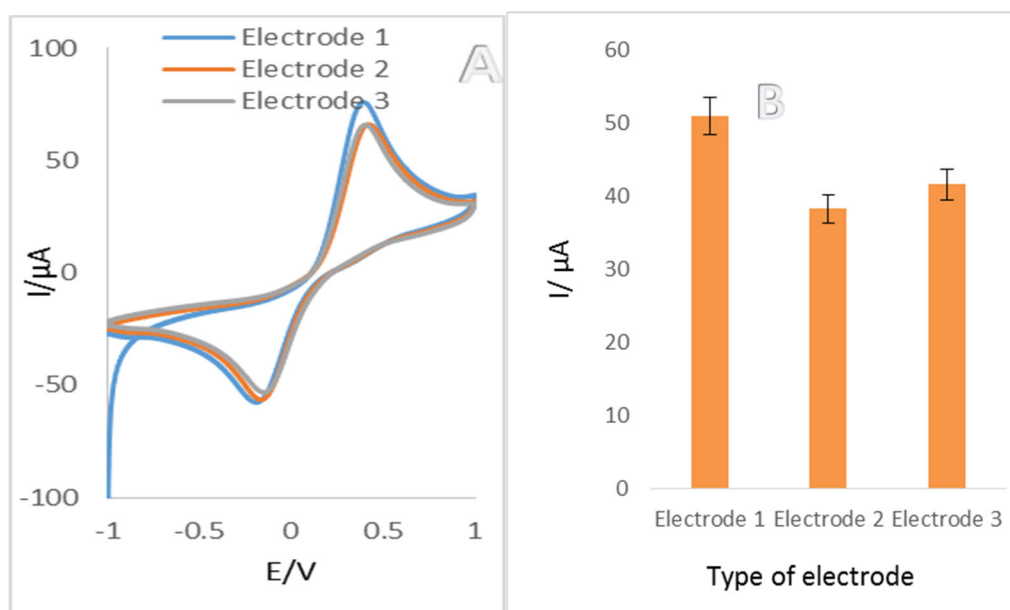**Figure S15. A)** CVs of aptasensor fabricated on three type of electrode with similar protocol. in 0.01 M $[Fe(CN)_6]^{3-/4-}$/KCl 0.01 M control solution. **B)** Related histogram for CV (n=3, SD=2.08).
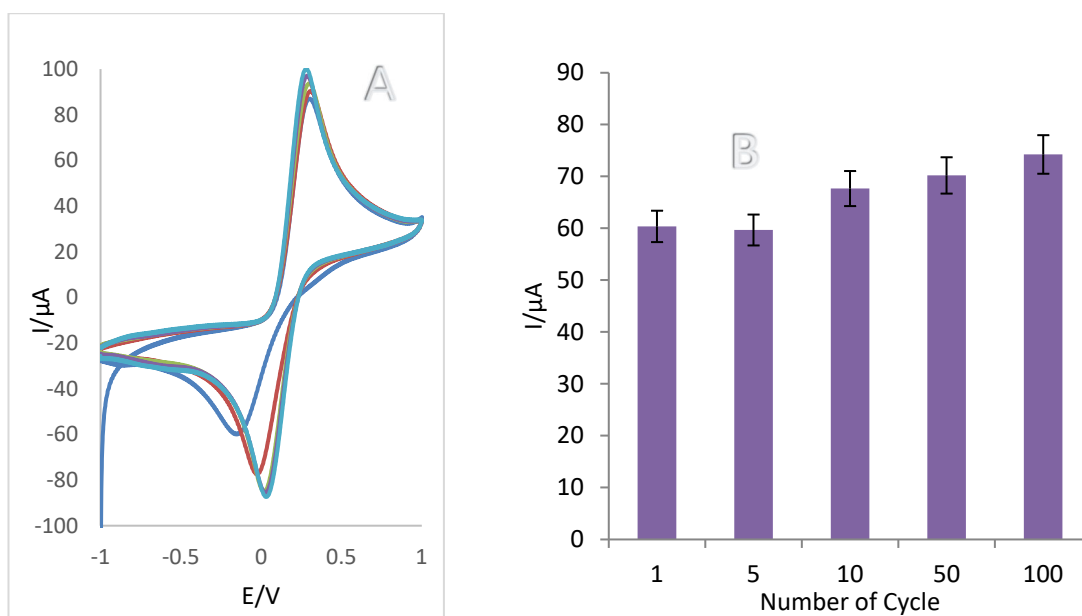

Figure S16. A) CVs of different cyclic (1, 5, 10, 50, and 100 cycles) study of aptamer/KCC-1-NH_2-DPA/P (β-CD)/Au electrode in the potential range -1 to 1 V and the scan rate of 100 mV/s. **B)** Histogram of peak current *versus* number of cycle (n=3, SD=2.00).
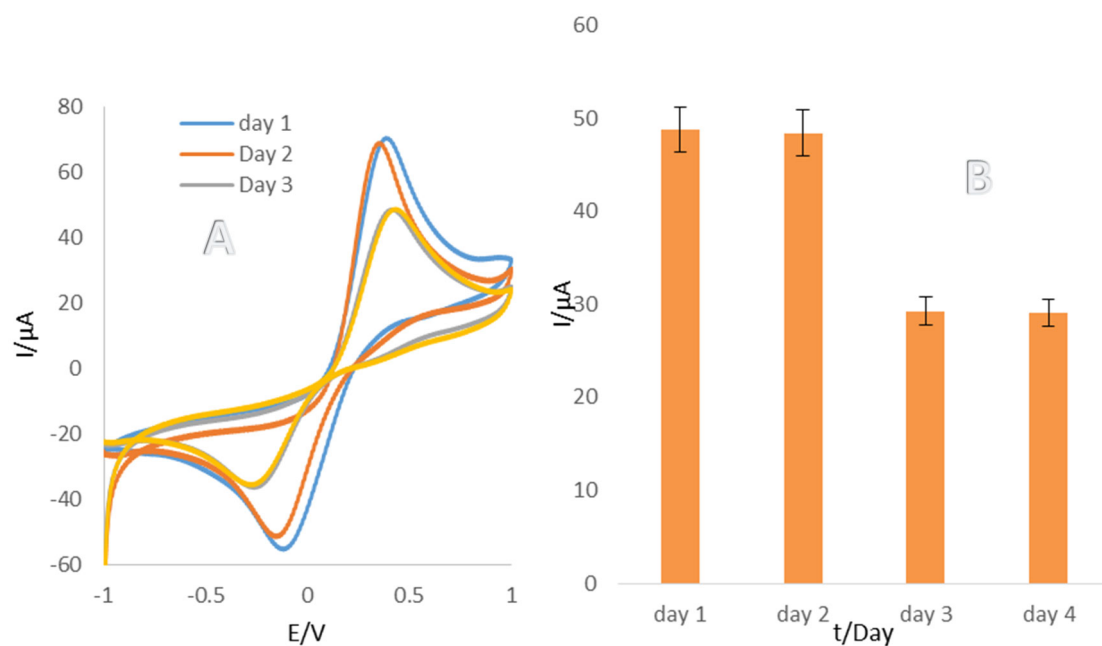
Figure S17. A) CVs of intraday assessment in 0.01 M $[Fe(CN)_6]^{3-/4-}$/KCl 0.01 M solution as electrolyte support and in the potential range -1 to 1 V and the scan rate of 100 mV/s. **B)** histogram of peak current *versus* time of storage (n=3, SD=1.97).

Reference

[1] S.M. Saadati, R. Zhiani, M. Zahedifar, S.M. Sadeghzadeh. *Appl. Organometallic Chem.* 32 (2018) e4560-e4569

[2] S.M. Sadeghzadeh, *RSC Adv.,* 6 (2016) 75973-75980

[3] K.E.A. AbouAitah, A.A. Farghali, A. Swiderska-Sroda, W. Lojkowski, A.M. Razin, M.K. Khedr, *J. Nanomed. Nanotechnol*. 7 (2016) 1-12.

[4] N. Bayal, B. Singh, R. Singh, V. Polshettiwar, *Sci. Rep.* 6 (2016) 24888-24896.

[5] S. Ge, Y. Zhang, L. Zhang, L. Liang, H. Liu, M. Yan, J. Huang, J. Yu, *Sens. Actuators B Chem.* 220 (2015) 665-672.

[6] S.M. Sadeghzadeh, *Catal. Commun.* 72 (2015) 91-96.